Title: Controlling the Amount of Co-catalyst as a Critical Factor in Determining the Efficiency of Photoelectrodes: The Case of Nickel (II) Hydroxide on Vanadate Photoanodes

Authors: Javier Quiñonero, Roberto Gómez

PII: S0926-3373(17)30548-9
DOI: http://dx.doi.org/doi:10.1016/j.apcatb.2017.06.005
Reference: APCATB 15745

To appear in: *Applied Catalysis B: Environmental*

Received date: 16-3-2017
Revised date: 31-5-2017
Accepted date: 3-6-2017

Please cite this article as: Javier Quiñonero, Roberto Gómez, Controlling the Amount of Co-catalyst as a Critical Factor in Determining the Efficiency of Photoelectrodes: The Case of Nickel (II) Hydroxide on Vanadate Photoanodes, Applied Catalysis B, Environmentalhttp://dx.doi.org/10.1016/j.apcatb.2017.06.005

Controlling the Amount of Co-catalyst as a Critical Factor in Determining the Efficiency of Photoelectrodes: The Case of Nickel (II) Hydroxide on Vanadate Photoanodes

Javier Quiñonero, Roberto Gómez*

Departament de Química Física i Institut Universitari d'Electroquímica

Universitat d'Alacant, Apartat 99, E-03080 Alicante, Spain

*Corresponding author. Tel: +34 96 590 3748; email address: roberto.gomez@ua.es

HIGHLIGHTS

- Nickel hydroxide behaves as an efficient co-catalyst for bismuth vanadate and iron vanadate photoanodes for water oxidation.
- Chemical bath deposition of nickel hydroxide allows for a fine control of the co-catalyst loading on the photoanode surface.
- Co-catalyst loading is critical for its performance, being optimal values of the order of only one monolayer.
- Electrochemical methods can be used to estimate the co-catalyst loading provided that it experiences a reversible redox behavior.

Abstract

A commonly followed strategy to enhance the performance of photoelectrodes for achieving viable water splitting devices consists in the use of co-catalysts. However, fine control of the amount of co-catalyst deposited on the electrode surface usually does not receive much attention, although it is an essential factor that crucially determines the efficiency of photoelectrodes. In this context, this study illustrates how the dark electrochemical characterization of co-catalyst-modified photoanodes may provide valuable information on the precise amount of electroactive co-catalyst present on the surface, facilitating our understanding of the manner in which co-catalysts work and paving the way for their optimization. For this purpose, ultrathin $Ni(OH)_2$ layers were deposited on either doped or pristine $BiVO_4$ and $FeVO_4$ photoanodes by a cost-effective and versatile chemical bath deposition method in which the deposition time allows to control the $Ni(OH)_2$ loading. The deposited $Ni(OH)_2$ is demonstrated to successfully catalyze the photoelectrochemical water oxidation process on both $BiVO_4$ and $FeVO_4$ electrodes, by improving the effective transfer of photogenerated holes from the semiconductor to solution. In fact, the electrocatalytic activity of the $Ni(OH)_2$-modified photoanodes rapidly increases with the amount of deposited $Ni(OH)_2$ until an optimum value is reached equivalent to only 0.46 and 1.68 $Ni(OH)_2$ monolayers for $BiVO_4$ and $FeVO_4$ electrodes, respectively. Under these conditions, $Ni(OH)_2$ enhances the photocurrent generation by a factor of 2 for $BiVO_4$ and of 1.2 for $FeVO_4$ photoanodes in contact with slightly alkaline solutions. The small loadings of $Ni(OH)_2$ leading to an optimum photoanode behavior indicate that hole transfer is favored on vanadate active surface sites, which would also be the preferential sites for $Ni(OH)_2$ deposition. Additional amounts of co-catalyst deposited for longer times induce a drastic decrease

in the $Ni(OH)_2$ photoelectrocatalytic activity due to charge recombination at the semiconductor/$Ni(OH)_2$ interface, probably enhanced by the low carrier mobility in $Ni(OH)_2$. On the other hand, this study demonstrates that the preparation of efficient photoanodes for oxygen evolution with an extremely small amount of co-catalyst through a facile and scalable method is possible.

Keywords: nickel hydroxide, chemical bath deposition, oxygen evolution reaction, photoelectrocatalysis, $BiVO_4$ photoanodes, $FeVO_4$ photoanodes.

1. Introduction

In order to overcome the current global warming caused by the employment of fossil fuels and the continuously growing energy consumption, the development of green, non-polluting and renewable alternative technologies for energy supply is desirable. In particular, since its discovery by Fujishima and Honda in 1972 [1], producing H_2 as a solar fuel from photoelectrochemical (PEC) water decomposition methodologies on semiconductor electrodes using only sunlight as input energy has been considered as an interesting goal [2–4]. In this context, the search for efficient semiconductor materials with potential application in the development of photoanodes capable of photooxidizing water has mainly focused on binary metal oxides for the last few decades, basically on TiO_2 (E_g = 3.2 eV, for the anatase phase) [5,6], WO_3 (E_g = 2.7 eV) [7,8] and Fe_2O_3 (E_g = 2.2 eV) [9–11]. However, this research has now been directed in part toward several ternary oxides, such as some tantalates [12–14], titanates [15–18] and wolframates [19–21], among others. These also include certain vanadates ($BiVO_4$ [22–25], $FeVO_4$ [26–28] and $InVO_4$ [29,30]), which are characterized by their electrical *n*-type properties, their relatively low cost and toxicity, intrinsic visible light activity, and acceptable chemical and photochemical stability in aqueous electrolytes.

Among the vanadates, $BiVO_4$ stands out as one of the most promising photoanode materials due to its convenient valence band edge, located at approximately 2.4 V (*vs*. RHE), which provides the necessary overpotential for photogenerated holes to oxidize water. It is also important to consider for visible light absorption its relatively narrow bandgap (2.4 eV for the monoclinic variety; although several other values are reported for other crystalline phases [22,31]). In addition, the poor carrier mobility observed for this semiconductor is compensated by a long carrier lifetime, which translates into a relatively long diffusion lengths for electrons and holes [32,33]. Similarly, iron vanadate ($FeVO_4$) is also a low bandgap semiconductor (for the triclinic structure, the E_g value is close to 2.06 eV), which facilitates the absorption of around 45% of the incident solar energy. In addition, it is composed of earth-abundant elements [28]. In any case, the actual conversion efficiency achieved with unmodified $BiVO_4$ and $FeVO_4$ is well below expectations. In fact, they present extremely poor photogenerated carrier transport properties, especially for electron transport in $BiVO_4$. The slow rates for driving complex reactions such as oxygen evolution, motivated by its high kinetic barrier and the extremely poor catalytic properties of the $BiVO_4$ and $FeVO_4$ surfaces are other important drawbacks for the use and applicability of these vanadates in photoelectrochemical devices [22,26,31].

Morphology control [34–36], heterojunction structure formation [37–39], and composition tuning have resulted in an enhancement of charge separation and transport in $BiVO_4$- [25,40–42] and $FeVO_4$-based [28] materials. However, the sluggish transfer of photogenerated holes to solution due to poor catalytic properties still remains as the main limiting factor for their use in water splitting. In addition, the resulting hole accumulation at the photoanode/electrolyte interface often results in photooxidation of the electrode (photocorrosion) [22]. In this way, the modification of the $BiVO_4$ surface

with oxygen evolution catalysts (OECs) has led to a dramatic improvement in the performance of the $BiVO_4$ photoanodes by accelerating the surface PEC water oxidation reaction kinetics and also by favoring charge separation through collection of photogenerated holes [43]. However, only a limited number of OECs are effective for $BiVO_4$ in PEC water oxidation, including certain transition metals and metal oxides (RuO_2 [43], Pt [44], IrO_x [44] PdO_x [45], CoO_x [46], NiO [47], Co_3O_4 [48] and RhO_2 [49]) and oxyhydroxides (such as FeOOH and NiOOH [50]) and some complex, ill-defined structures known as 'cobalt phosphate' (Co-Pi) [51], 'cobalt carbonate' (Co-Ci) [52] and 'nickel-borate' (Ni-Bi) [53]. To the best of our knowledge, no OEC incorporation has been reported to date in the case of $FeVO_4$ photoanodes.

The interest in Ni^{3+}-based OECs for (photo)electrocatalysis, such as $NiOOH/Ni(OH)_2$, is due to the fact that Ni^{3+} is particularly catalytic for a wide range of redox processes [54]. In fact, the electrocatalytic properties of NiOOH have been studied and confirmed, not only for oxygen evolution reaction (OER) in PEC water splitting [50,55,56], but also in a wide range of reactions, such as the oxidation of alcohols to yield carbonyl compounds [57–60], the direct electrooxidation of carbohydrates [61] and urea [62] and a green route oxidation of sulfide ions [63]. The electrocatalytic effect has been primarily attributed by Trotochaud *et al.* to Fe contamination, which plays a critical role in enhancing the activity of the Ni-based OER electrocatalysts [64], but it is also thought to be motivated by the low degree of occupancy of the *d* orbitals associated with the Ni oxidized form (NiOOH). In fact, the metal ion in its high valence state has more activity for bond formation with adsorbed species, thus facilitating electrocatalytic activity [65–67]. The importance of studying the OER over $Ni(OH)_2$ in alkaline media derives from the fact that the best OECs in acid media (RuO_2 and IrO_2) suffer from poor chemical stability in basic solutions [68]. Although $Ni(OH)_2$ possesses a lower

electrocatalytic activity, it displays excellent long term corrosion resistance in basic solutions and it has the added advantage of being relatively inexpensive.

In this work, transparent $Ni(OH)_2$ ultrathin films have been deposited on pristine and doped $BiVO_4$ as well as on $FeVO_4$ photoanodes by a chemical bath deposition (CBD) method to study their activity as OEC in PEC water oxidation. The deposition method, besides being cost-effective, is scalable and extremely versatile since it should also be practical for large-area deposition and successfully applicable in the case of a wide range of materials beyond bismuth and iron vanadates. It offers the possibility of achieving a well-defined $Ni(OH)_2$ structure by controlling the amount of deposited co-catalyst in an effective way by changing only the deposition time and monitoring the amount of deposited $Ni(OH)_2$ by cyclic voltammetry. In such a way, it is possible to quantify the surface density of co-catalyst needed for an optimum electrode PEC performance. Surface modification of $BiVO_4$ and $FeVO_4$ with $Ni(OH)_2$ layers also enhances their chemical and photoelectrochemical stability in alkaline solutions, a much more convenient working media from the standpoint of their practical applicability in water splitting devices [69].

2. Experimental section.

2.1. Preparation of $BiVO_4$ photoanodes. Pristine $BiVO_4$ thin film photoanodes were prepared on fluorine-doped tin oxide (F:SnO_2, FTO, U-type 12 Ω^2, Asahi Glass Co.) by a previously reported procedure based on a modified metal-organic decomposition method (MOD) followed by a thermal degradation of the corresponding metal-organic precursor [70]. Bi and V precursor solutions were prepared by dissolving $Bi(NO_3)_3 \cdot 5H_2O$ (Sigma-Aldrich, 98%) 0.2 M and $VO(C_5H_7O_2)_2$ (Fluka Analytical, 97%) 0.03 M in acetic acid (Scharlau, 99%) and acetylacetone (Fluka Analytical, 99.5%), respectively. They were mixed in a 1:1 mole ratio of Bi to V to obtain the

corresponding $BiVO_4$ precursor solution. Then, 40 μL of the mixed solution was dropped onto an FTO glass plate (area to be covered: 1 cm^2), previously cleaned by 15-min sonication (Selecta Ultrasonics) in acetone (Panreac, P.A.) and ethanol (VWR Prolabo Chemicals, 96%), and spread over it with a spin-coater (Chemat Technology, KW-4A) at a spin rate of 1500 rpm for 10 s. Finally, the electrodes were annealed at 500ºC for 30 min in air, with a heating rate of 5ºC·min^{-1}, using a programmable furnace (Conatec, 7800). This procedure was repeated six times to achieve the optimum $BiVO_4$ film thickness.

2.2. Preparation of doped $BiVO_4$ photoanodes. La (1 at%)- and Ce (2 at%)-doped $BiVO_4$ thin film photoanodes were obtained following the same procedure described above, but incorporating the doping element in the $BiVO_4$ precursor solution at the desired concentration (in at% with respect to either Bi or V content) [70]. In this case, $La(NO_3)_3 \cdot 6H_2O$ (Fluka Analytical, 99%) and $Ce(NO_3)_3 \cdot 6H_2O$ (Strem Chemicals, 99%) were employed as La and Ce precursors, respectively.

2.3. Preparation of $FeVO_4$ photoanodes. $FeVO_4$ thin film photoanodes were also synthesized by layer-by-layer coating over conducting FTO glass substrates through a modified MOD method followed by a thermal treatment [28]. The $FeVO_4$ precursor solution was prepared by mixing $Fe(NO_3)_3 \cdot 9H_2O$ (Merck, 99%) and $VO(C_5H_7O_2)_2$ (Fluka Analytical, 97%), in equimolar 0.2 M concentration, in a 10-mL solution of acetic acid (Scharlau, 99%) and acetylacetone (Fluka Analytical, 99.5%) (1:8.25 by v/v) that was magnetically stirred for 24 h. The resulting solution was then spun on clean FTO glass substrates (40 μL for an area to be covered of 1 cm^2) at 1000 rpm for 30 s and subsequently annealed at 250ºC for 10 min (heating rate: 5ºC·min^{-1}). This process was repeated five times, and then, the films were annealed in two stages: a first annealing at 500ºC for 30 min was applied to combust the organic compounds and to

improve the contact among the particles and with the substrate, and a second annealing at 550ºC for 1 h to obtain the final films. These heat treatments were also done in air with a heating rate of 5ºC·min^{-1}.

2.4. $Ni(OH)_2$ surface deposition on pristine and doped $BiVO_4$ and $FeVO_4$ photoanodes. $Ni(OH)_2$ was deposited on pristine and doped $BiVO_4$ and $FeVO_4$ photoanodes by a CBD procedure [56]. The deposition solution contained 25 mL of 0.5 M $NiSO_4$·6-7H_2O (Riedel-de Haën, for nickel plating), 12.5 mL of 1 M urea (Sigma-Aldrich, P.A.) and 12.5 mL of H_2O (Millipore, Essential Elix 3). The FTO substrates were vertically supported with the conducting side (either bare or covered with $BiVO_4$ or $FeVO_4$) faced against the beaker wall, and the solution was heated up to 100ºC in a stove (Memmert, 100-800). Different deposition times (from 10 to 50 min) were assayed as to control the amount of deposited $Ni(OH)_2$. After deposition, the samples were rinsed with distilled water, air dried and annealed at 200ºC in air for 1 h (heating rate: 5ºC·min^{-1}). This heat treatment does not induce the dehydrogenation of the deposited $Ni(OH)_2$ [71].

2.5. Photoanode characterization and photoelectrochemical measurements. A SEM study was carried out to characterize the surface morphology of the films using a ZEISS Merlin VP Compact field emission scanning electron microscope (FESEM). TEM micrographs were obtained with a JEOL transmission electron microscope JEM-2010. For the surface composition study of the films, XPS experiments were done with a Thermo-Scientific K-Alpha XPS spectrometer equipped with a monochromatic Al-Kα source (1486.6 eV), operating at 15 kV and 10 mA.

PEC measurements were conducted at room temperature in a home-made Pyrex glass cell with a fused silica window and a computer-controlled potentiostat-galvanostat (Autolab, PGSTAT30). A Pt wire and an Ag/AgCl/KCl(3 M) electrode were used as the

counter and reference electrodes, respectively. Unless otherwise stated, all the potentials are referred to this Ag/AgCl electrode. An N_2-purged NaB_i (pH = 10.0) buffer solution was used as the working electrolyte for the (photo)electrochemical measurements. The light source was an ozone-free 1000 W Xe(Hg) lamp (Newport Instruments, 66921) equipped with a water filter to minimize the infrared contribution of the beam, and all the PEC measurements were carried out by irradiating the prepared photoanodes through the electrolyte/electrode interface (EE illumination). The photon flux intensity was measured by means of a photodiode power meter (Thorlabs, PM100D), and the typical value was approximately 100 $mW \cdot cm^{-2}$.

3. Results and discussion.

3.1. Pristine and La- and Ce-doped $BiVO_4$ photoanodes modified with $Ni(OH)_2$. Fig. 1 shows the electrochemical characterization in the dark for $BiVO_4/Ni(OH)_2$ photoanodes prepared for different $Ni(OH)_2$ deposition times (from 10 to 50 min), together with the corresponding response for $FTO/Ni(OH)_2$ electrodes synthesized for the same deposition times. The voltammetric behavior of the $BiVO_4$ substrate is characterized by the appearance of *quasi*-reversible pseudocapacitive signals at potentials below -0.2 V, which is attributed to redox processes undergone by V surface atoms. Importantly, the voltammetric profiles are stable over a wide potential range, which suggests stability of the $BiVO_4$ film. Voltammograms for bare pristine and doped $BiVO_4$ electrodes are shown in Fig. S1. As the $Ni(OH)_2$ deposition proceeds, a cathodic peak grows at approximately 0.65 V, which is associated with the redox process:

$$NiOOH + H_2O + e^- \longrightarrow Ni(OH)_2 + OH^- \qquad \text{Eq. (1)}$$

Doped $BiVO_4$ electrodes show the same voltammetric behavior for different $Ni(OH)_2$ deposition times as shown in Figs. S2 and S3.

As expected, the charge associated to the Ni reduction peak (q_{Ni}) increases with the $Ni(OH)_2$ deposition time (Fig. 2a). The deposition of $Ni(OH)_2$ on the $BiVO_4$ and FTO surfaces has a direct effect on the electrochemical behavior of these electrodes in the region of positive potentials. In fact, immediately above 0.7 V, significant faradaic currents, attributable to oxygen evolution in the dark, are observed. These currents increase with the amount of deposited $Ni(OH)_2$ (Fig. 2b). From the curves in Fig. 2a, it is evident that the nucleation rate of $Ni(OH)_2$ on both surfaces is rather slow and their subsequent growth is significantly faster for the FTO substrate. On the other hand, the OER activity tends to saturate for relatively large amounts of $Ni(OH)_2$. Interestingly, for low $Ni(OH)_2$ amounts, the vanadate substrate slightly enhances the OER catalytic effect over that of the bare FTO case, which is particularly relevant for the use of $Ni(OH)_2$ as a co-catalyst.

Linear scan voltammograms recorded under transient illumination for $BiVO_4/Ni(OH)_2$, La (1 at%)-$BiVO_4/Ni(OH)_2$ and Ce (2 at%)-$BiVO_4/Ni(OH)_2$ prepared for different $Ni(OH)_2$ deposition times (from 0 to 50 min) (Fig. 3 and Fig. S4) are characterized by the existence of very small dark currents together with stable anodic photocurrents whose magnitude is clearly deposition-time dependent. The maximum value of the photocurrent is obtained for a deposition time of 20 min. For longer times (30 min and beyond), a drastic decrease in the magnitude of the photocurrent is observed. This reduction in photocurrent is accompanied by a significant intensification of the anodic and cathodic spikes observed upon illumination/light interruption. This is a clear sign of electron-hole recombination induced by hole trapping in the relatively thick $Ni(OH)_2$ layer deposited on the photoanode surface: although initially the separation of the photogenerated charges takes place, holes are trapped likely at the $BiVO_4/Ni(OH)_2$ interface, favoring recombination. In fact, charge transport through

$Ni(OH)_2$ is not efficient due to its low electrical conductivity, which implies that ultrathin $Ni(OH)_2$ layers are required for a fast hole transfer to solution and a subsequent good (photo)electrocatalytic performance. It is also worth noting that the incorporation of the catalyst does not induce any displacement of the photoonset value, which is located at around -0.8 V *vs*. Ag/AgCl (0.0 V *vs*. RHE).

Chronoamperometric measurements for pre-optimum (10 min), optimum (20 min) and post-optimum (30 min) $Ni(OH)_2$ deposition times for $BiVO_4/Ni(OH)_2$ (Fig. 4a-c) at -0.5 V (*i. e.*, close to the photocurrent onset) confirm the tendencies already observed in the voltammetric experiments. Concretely, Fig. 4d shows a plot of the photocurrent recorded at -0.5 V for $BiVO_4/Ni(OH)_2$ photoanodes *vs*. the charge density corresponding to the reduction of NiOOH. The same tendency, although less marked, is observed for other values of applied potential. This plot shows how the photocurrent magnitude varies as a function of the amount of Ni, which, in turn, is dependent on the $Ni(OH)_2$ deposition time. The optimum is located at a q_{Ni} of approximately 125 $\mu C \cdot cm^{-2}$ (for a deposition time equal to 20 min). This value corresponds to a Ni atom surface density of $5.4 \cdot 10^{14}$ cm^{-2}. By using the q_{Ni} value corresponding to one monolayer (ML) as defined in a previous study [56], a second *x*-axis is added to Fig. 4d, indicating in an explicit way the number of equivalent monolayers for the different studied samples. Strikingly, the optimum co-catalyst coverage is as low as 0.46 ML. We should emphasize that the coverage calculation is done by assuming that the surface is perfectly flat, which is not the case (see below). The actual coverage that would be calculated on the basis of the real surface area would be substantially smaller. Such a low optimum coverage clearly illustrates the concept of active site as only a minor fraction of the $BiVO_4$ surface sites seems to be relevant in the trapping and transfer of holes to the electrolyte. On the other hand, the low optimum $Ni(OH)_2$ coverage is also a result of the

poor charge transport properties of $Ni(OH)_2$/NiOOH. The existence of a region with a $Ni(OH)_2$ deposit with a thickness equivalent to several monolayers would be deleterious for the final hole transfer to solution.

In the same way, the surface density of co-catalyst needed for an optimum electrode PEC performance is estimated to be around $1.2 \cdot 10^{15}$ and $1.4 \cdot 10^{15}$ Ni atoms/cm^2 for La (1 at%)- and Ce (2 at%)-doped $BiVO_4$ photoanodes, which corresponds to 0.99 and 1.2 ML, respectively. The significant difference in the optimum Ni atom surface density between pristine and doped electrodes could be attributed to the fact that, in the doped samples, there would be more surface active centers as a consequence of the doping procedure than in the case of pristine $BiVO_4$.

Fig. 5a-d displays top view FESEM images for a bare $BiVO_4$ sample and $BiVO_4$ samples modified with $Ni(OH)_2$ for deposition times of 10, 20 and 30 min (see Fig. S5a for a $BiVO_4$ cross-sectional FESEM image showing a vanadate film thickness of about 0.4 μm). From the comparison of these FESEM micrographs, no significant differences are observed in the electrode morphology upon modification with $Ni(OH)_2$ for the studied deposition times. Only in the case of the $BiVO_4$ sample modified with $Ni(OH)_2$ (deposition time of 30 min), the appearance of an overstructure in the form of acicular particles corresponding to the $Ni(OH)_2$ deposit on the relatively rough surface of the $BiVO_4$ substrate starts to be discerned (see encircled area in Fig. 5d). It is also important to note that Fig. 5a-d and particularly Fig. S5a evince the compact nature of the $BiVO_4$ film, which precludes the existence of $Ni(OH)_2$ in direct contact with the substrate. Selected TEM micrographs (Fig. 5e-h) do reveal the existence of the $Ni(OH)_2$ deposit more clearly. Comparing images obtained for a bare $BiVO_4$ sample (Fig. 5e) with those corresponding to samples modified with $Ni(OH)_2$ for deposition times of 10, 20 and 30 min (Fig. 5f-h), the existence of $Ni(OH)_2$ deposits of different thickness on the surface

of $BiVO_4$ photoanodes can be verified. This $Ni(OH)_2$ deposit grows as the deposition time increases and it consists of particles with an elongated morphology and small dimensions. It is worth noting that the selected TEM images in Fig. 5 are those revealing more clearly the existence of the $Ni(OH)_2$ deposit. In any case, it should be emphasized that the average $Ni(OH)_2$ layer thickness for deposition times of 10, 20 and 30 min is extremely low (that is, only ultrathin films are generated). In fact, EDX analysis of the samples could not detect the presence of Ni whose concentration is thus below the detection limit of the equipment.

It can then be assumed that, for submonolayer and monolayer coverages, most of the deposited nickel atoms are distributed in small clusters or islands. These isolated $Ni(OH)_2$ islands would be able to quickly exchange photogenerated holes with the electrolyte as the fraction of nickel atoms exposed to the electrolyte would be maximum. By trapping holes photogenerated in the semiconductor, surface Ni^{2+} would locally oxidize to Ni^{3+}. Only a minor fraction of these Ni^{3+} centers would be further oxidized to Ni^{4+} due to the trapping of a second photogenerated hole. The Ni^{4+} species are supposed to act as the actual electrocatalytic centers, finally transferring the hole to solution and participating in the oxidation of water to O_2, with its subsequent reduction to Ni^{3+} (Fig. 6). However, as coverage grows (for $Ni(OH)_2$ deposition times of 30 min and beyond), an increasing fraction of the deposited Ni atoms would be in second and successive monolayers, not in direct contact with the electrolyte, being thus less effective for promoting the OER. This fact, together with the rather low electrical conductivity of the increasingly thick $Ni(OH)_2$ deposit, would cause a drastic decrease in their activity as co-catalyst, preventing the exchange of charges with solution and enhancing electron-hole recombination. It is finally relevant to mention that with a very

low deposited amount, invoking a preferential transfer of the holes to the $Ni(OH)_2$ phase is not sound, being the role of the $Ni(OH)_2$ (sub)monolayer almost exclusively catalytic.

Fig. 7 shows a comparison between the initial and final (before and after the photoelectrochemical characterization, respectively) voltammetric measurements in the dark for these electrodes in an N_2-purged NaB_i buffer solution (pH = 10.0). No important differences in the shape of the corresponding voltammograms are observed, and the charge density exchanged in the NiOOH reduction process remains almost constant before and after the photoelectrochemical characterization. This is particularly significant on account of the very low amounts of deposited $Ni(OH)_2$. These results point to a significant stability of the electrodes in alkaline solutions.

Fig. 8 contains Ni 2*p* XPS spectra for $BiVO_4/Ni(OH)_2$, La (1 at%)-$BiVO_4/Ni(OH)_2$ and Ce (2 at%)-$BiVO_4/Ni(OH)_2$ photoanodes, prepared for a $Ni(OH)_2$ deposition time of 20 min. In the three cases, the XPS spectrum of Ni shows two main peaks with binding energies (E_b) of around 855.9 eV and 873.5 eV, corresponding to the Ni $2p_{3/2}$ and $2p_{1/2}$ transitions [56], respectively, and one 2*p* satellite band [53] at 862 eV. The accurate determination of the specific Ni oxidation state is usually difficult as there are diverse binding energies for the same Ni oxidation state (Ni^{2+} and Ni^{3+}) within a range of 1 eV [53]. However, in this case, the clear shift of Ni $2p_{3/2}$ peaks to higher E_b values with respect to those typical for NiO [72–74] and the absence of peaks attributable to Ni in its oxidized form (NiOOH) provide evidence that, as expected, the deposit over the prepared samples is completely composed of $Ni(OH)_2$. According to the XPS quantitative analysis, the Ni content (in at%) on the $BiVO_4/Ni(OH)_2$, La (1 at%)-$BiVO_4/Ni(OH)_2$ and Ce (2 at%)-$BiVO_4/Ni(OH)_2$ studied samples is 1.22, 1.63 and 2.06 at%, respectively. These results are consistent with the amounts of Ni obtained from electrochemical measurements, which are larger for the doped samples than for pristine

$BiVO_4$. XPS spectra for Bi 4*f*, V 2*p*, O1*s*, La 3*d* and Ce 3*d* are given in the Supplementary Materials (Figs. S6-S8).

3.2. $FeVO_4$ photoanodes modified with $Ni(OH)_2$. The XRD pattern for $FeVO_4$ deposited on FTO (Fig. S9) presents weak reflections corresponding to the main lines of the triclinic polymorph, thus confirming its crystalline structure. As shown in Fig. 9a, a FESEM image of the $FeVO_4$ surface reveals that the deposit exhibits the typical morphology of a thin film characterized by a low porosity and a high compactness (see Fig. S5b for a $FeVO_4$ cross-sectional FESEM image). The linear scan voltammogram under transient illumination presented in Fig. 9b shows the existence of small dark currents (in agreement with the cyclic voltammogram also shown in Fig. 9b) together with anodic photocurrents over a wide potential range. The photocurrent, whose magnitude increases with increasing applied potentials, confirms an *n*-type electrical character for the prepared semiconductor film, which is remarkably stable. The photoonset potential is located, approximately, at -0.1 V, which agrees with previous studies [28].

The deposition of $Ni(OH)_2$ on $FeVO_4$ photoanodes has also been studied (Fig. 10). Upon depositing different amounts of $Ni(OH)_2$, an electrochemical behavior similar to that discussed for $BiVO_4$ electrodes is observed. In fact, a growing cathodic peak in the corresponding cyclic voltammetry in the dark linked to the NiOOH reduction process appears at approximately 0.65 V as $Ni(OH)_2$ deposition proceeds (Fig. 10a-e). This leads to a subsequent improvement in the magnitude of the photocurrents for the $FeVO_4/Ni(OH)_2$ electrode until a maximum enhancement is reached for a $Ni(OH)_2$ deposition time of 20 min. For $Ni(OH)_2$ deposition times above 30 min, a significant decrease in the magnitude of the photocurrent is observed, together with the appearance of anodic and cathodic spikes upon illumination/light interruption. The deposition of

$Ni(OH)_2$ does not induce any displacement of the photoonset, which remains located at -0.1 V (Fig. 10f-j).

As previously discussed, the voltammetric signals for the presence of $Ni(OH)_2$ which are present in the cyclic voltammograms in the dark in Fig. 10a-e allows for an accurate determination of the deposited co-catalyst amount. In this way, Fig. 11 shows a plot of the photocurrent recorded at 0.1 V for $FeVO_4/Ni(OH)_2$ photoanodes *vs*. the charge density corresponding to the reduction of NiOOH for samples with different loadings of $Ni(OH)_2$. The optimum coverage (see Fig. S10 for a FESEM image) corresponds to a charge density of approximately 450 $\mu C \cdot cm^{-2}$ (for a deposition time equal to 20 min), which is equivalent to around 1.68 $Ni(OH)_2$ ML. It is worth noting that the amount of deposited $Ni(OH)_2$ inducing the maximum enhancement in the photocurrent values is significantly larger than that required for pristine $BiVO_4$. This could be simply linked to the fact that the surface roughness of $FeVO_4$ appears to be larger than that of $BiVO_4$.

4. Conclusions.

This study aims to illustrate the need for a careful control of the amount of co-catalyst deposited on the photoelectrode surface as a key factor determining its efficiency, as well as the usefulness of electrochemical methods for monitoring such an amount. For this purpose, ultrathin $Ni(OH)_2$ layers have been deposited on pristine and doped $BiVO_4$ as well as on pristine $FeVO_4$ photoanodes by means of a urea-based chemical bath deposition method that allows for a straightforward and fine control of the quantity of deposited co-catalyst. By controlling the deposition time, photoanodes surface-modified with different amounts of $Ni(OH)_2$ have been prepared and their electrocatalytic activity studied and discussed as a function of the amount of deposited $Ni(OH)_2$. Cyclic scan

voltammograms in the dark provide clear voltammetric signals associated with $Ni(OH)_2$, allowing for an accurate determination of its loading, while linear scan voltammograms under transient illumination offer insights into the photoactivity for the oxygen evolution reaction of the as-fabricated photoanodes.

The electrocatalytic activity of the $Ni(OH)_2$-modified $BiVO_4$ photoanodes rapidly increases with the amount of deposited $Ni(OH)_2$ until an optimum value is reached (for 20 min of $Ni(OH)_2$ deposition in all cases). The coverage values that enable an optimum PEC performance have been calculated to be 0.46, 0.99 and 1.2 equivalent $Ni(OH)_2$ monolayers, for pristine, La (1 at%)- and Ce (2 at%)-doped $BiVO_4$ photoanodes, respectively. In the case of the $FeVO_4$ electrodes, the highest enhancement in the values of the recorded photocurrents is achieved with 1.68 equivalent $Ni(OH)_2$ monolayers.

The enhancement observed upon $Ni(OH)_2$ deposition results from the fact that the $Ni(OH)_2$ deposit acts as an oxygen evolution catalyst, favoring the transfer of photogenerated holes through the electrode/electrolyte interface. In fact, when the amount of co-catalyst over the photoanode surface is low, most of the deposited nickel atoms act as active catalytic centers for hole transfer to solution as they should be distributed in monolayer-high islands and directly exposed to the electrolyte. However, thicker $Ni(OH)_2$ layers, obtained for longer deposition times (above 30 min), induce a drastic decrease in the electrocatalytic activity. This is attributed to the fact that an increasing number of deposited Ni atoms would not act as active catalytic centers but as recombination centers, as they are not in direct contact with the electrolyte. This together with the poor charge transport capabilities of the $Ni(OH)_2$ deposit leads to enhanced charge recombination at the semiconductor/$Ni(OH)_2$ interface. It is worth noting that the low value of the optimum $Ni(OH)_2$ coverage also illustrate clearly the concept of surface active site in photoelectrocatalysis.

In more general vein, this study shows that the modification of vanadate electrodes with optimized $Ni(OH)_2$ loadings enables their potential practical application as efficient photoanodes in water splitting devices while using minimum amounts of Ni-based co-catalyst. In fact, the possibility of using a method that allows the slow and controlled deposition of extremely small amounts of co-catalyst, as shown here, can also enable the practicality of more expensive co-catalysts, such as IrO_x or RhO_2.

Acknowledgements.

Financial support of the Spanish Ministry of Economy and Competitiveness through project MAT2015-71727-R (FONDOS FEDER) is gratefully acknowledged. J. Q. thanks the Generalitat Valenciana CEICE as well as the Spanish Ministry of Education, Culture and Sport for the award of ACIF and FPU predoctoral grants, respectively.

References.

[1] A. Fujishima, K. Honda, Nature. 238 (1972) 37–38.

[2] T. Bak, J. Nowotny, M. Rekas, C. Sorrell, Int. J. Hydrogen Energy. 27 (2002) 991–1022.

[3] A. B. Murphy, P. R. F. Barnes, L. K. Randeniya, I. C. Plumb, I. E. Grey, M. D. Horne, J. A. Glasscock, Int. J. Hydrogen Energy. 31 (2006) 1999–2017.

[4] M. G. Walter, E. L. Warren, J. R. McKone, S. W. Boettcher, Q. Mi, E. A. Santori, N. S. Lewis, Chem. Rev. 110 (2010) 6446–6473.

[5] T. Berger, D. Monllor-Satoca, M. Jankulovska, T. Lana-Villarreal, R. Gómez, ChemPhysChem. 13 (2012) 2824–2875.

[6] F. Han, V. S. R. Kambala, M. Srinivasan, D. Rajarathnam, R. Naidu, Appl. Catal. A. 359 (2009) 25–40.

[7] J. A. Seabold, K. S. Choi, Chem. Mater. 23 (2011) 1105–1112.

[8] C. Santato, M. Odziemkowski, M. Ulmann, J. Augustynski, J. Am. Chem. Soc. 123 (2001) 10639–10649.

[9] K. Sivula, F. L. Formal, M. Grätzel, ChemSusChem. 4 (2011) 432.

[10] I. Cesar, K. Sivula, A. Kay, R. Zboril, M. Grätzel, J. Phys. Chem. C. 113 (2009) 772–782.

[11] I. Cesar, A. Kay, J. A. G. Martinez, M. Grätzel, J. Am. Chem. Soc. 128 (2006) 4582–4583.

[12] H. Kato, A. Kudo, J. Phys. Chem. B. 105 (2001) 4285–4292.

[13] H. Kato, A. Kudo, Chem. Phys. Lett. 295 (1998) 487–492.

[14] H. Kato, A. Kudo, Catal. Letters. 58 (1999) 153–155.

[15] T. Watanabe, A. Fujishima, K. Honda, Bull. Chem. Soc. Jpn. 49 (1976) 355–358.

[16] M. S. Wrighton, A. B. Ellis, P. T. Wolczanski, D. L. Morse, H. B. Abrahamson, D. S. Ginley, J. Am. Chem. Soc. 98 (1976) 2774–2779.

[17] H. G. Kim, O. S. Becker, J. S. Jang, S. M. Ji, P. H. Borse, J. S. Lee, J. Solid State Chem. 179 (2006) 1214–1218.

[18] J. H. Kennedy, J. K. W. Frese, J. Electrochem. Soc. 123 (1976) 1683–4686.

[19] K. J. Pyper, T. C. Evans, B. M. Bartlett, Chinese Chem. Lett. 26 (2015) 474–478.

[20] J. Zhu, W. Li, J. Li, Y. Li, H. Hu, Y. Yang, Electrochim. Acta. 112 (2013) 191–198.

[21] J. Yourey, K. Pyper, J. Phys. Chem. 117 (2013) 8707–8718.

[22] Y. Park, K. J. McDonald, K.-S. Choi, Chem. Soc. Rev. 42 (2013) 2321–2337.

[23] S. P. Berglund, D. W. Flaherty, N. T. Hahn, A. J. Bard, C. B. Mullins, J. Phys. Chem. C. 115 (2011) 3794–3802.

[24] Z.-F. Huang, L. Pan, J.-J. Zou, X. Zhang, L. Wang, Nanoscale. 6 (2014) 14044–14063.

[25] K. Sayama, A. Nomura, T. Arai, T. Sugita, R. Abe, T. Oi, Y. Iwasaki, Y. Abe, H. Sugihara, J. Phys. Chem. B. 110 (2006) 11352–11360.

[26] C. D. Morton, I. J. Slipper, M. J. K. Thomas, B. D. Alexander, J. Photochem. Photobiol. A Chem. 216 (2010) 209–214.

[27] H. Mandal, S. Shyamal, P. Hajra, A. Bera, D. Sariket, S. Kundu, S. Bhattacharya, RSC Adv. 6 (2016) 4992–4999.

[28] S. K. Biswas, J. O. Baeg, Int. J. Hydrogen Energy. 38 (2013) 14451–14457.

[29] C. S. Enache, D. Lloyd, M. R. Damen, J. Schoonman, R. Van De Krol, J. Phys. Chem. C. 113 (2009) 19351–19360.

[30] J. Ye, Z. Zou, M. Oshikiri, A. Matsushita, Chem. Phys. Lett. 356 (2002) 221–226.

[31] Z.-F. Huang, L. Pan, J.-J. Zou, X. Zhang, L. Wang, Nanoscale. 6 (2014) 14044–14063.

[32] F. F. Abdi, T. J. Savenije, M. M. May, B. Dam, R. Van De Krol, J. Phys. Chem. Lett. 4 (2013) 2752–2757.

[33] A. J. E. Rettie, W. D. Chemelewski, D. Emin, C. B. Mullins, J. Phys. Chem. Lett. 7 (2016) 471–479.

[34] W. Luo, Z. Wang, L. Wan, Z. Li, T. Yu, Z. Zou, J. Phys. D. Appl. Phys. 43 (2010) 405402.

[35] G. Xi, J. Ye, Chem. Commun. 46 (2010) 1893–1895.

[36] J. Su, L. Guo, N. Bao, C. A. Grimes, Nano Lett. 11 (2011) 1928–1933.

[37] Y. H. Ng, A. Iwase, A. Kudo, R. Amal, J. Phys. Chem. Lett. 1 (2010) 2607–2612.

[38] P. Chatchai, Y. Murakami, S. Kishioka, A. Y. Nosaka, Y. Nosaka, Electrochim. Acta. 54 (2009) 1147–1152.

[39] X. Liu, Y. Kang, Mater. Lett. 164 (2016) 229–231.

[40] W. Yao, H. Iwai, J. Ye, Dalton Trans. 11 (2008) 1426–1430.

[41] H. W. Jeong, T. H. Jeon, J. S. Jang, W. Choi, H. Park, J. Phys. Chem. C. 117 (2013) 9104–9112.

[42] X. Zhang, X. Quan, S. Chen, Y. Zhang, J. Hazard. Mater. 177 (2010) 914–917.

[43] J. Yang, D. Wang, H. Han, L. Can, Acc. Chem. Res. 46 (2013) 1900–1909.

[44] H. Ye, H. S. Park, A. J. Bard, J. Phys. Chem. C. 115 (2011) 12464–12470.

[45] J. H. Kim, J. W. Jang, H. J. Kang, G. Magesh, J. Y. Kim, J. H. Kim, J. Lee, J. S. Lee, J. Catal. 317 (2014) 126–134.

[46] M. F. Lichterman, M. R. Shaner, S. G. Handler, B. S. Brunschwig, H. B. Gray, N. S. Lewis, N. S. Spurgeon, J. Phys. Chem. Lett. 4 (2013) 4188–4191.

[47] S. Xie, T. Zhai, Y. Zhu, W. Li, R. Qiu, Y. Tong, X. Lu, Int. J. Hydrogen Energy. 39 (2014) 4820–4827.

[48] M. Long, W. Cai, H. Kisch, J. Phys. Chem. C. 112 (2008) 548–554.

[49] Z. Li, W. Luo, M. Zhang, J. Feng, Z. Zou, Energy Environ. Sci. 6 (2013) 347–370.

[50] T.W. Kim, K.-S. Choi, Science 343 (2014) 990–994.

[51] T. H. Jeon, W. Choi, H. Park, Phys. Chem. Chem. Phys. 13 (2011) 21392–21401.

[52] C. Ding, J. Shi, D. Wang, Z. Wang, N. Wang, G. Liu, F. Xiong, Phys. Chem. Chem. Phys. 15 (2013) 4589–4595.

[53] S. K. Choi, W. Choi, H. Park, Phys. Chem. Chem. Phys. 15 (2013) 6499–507.

[54] J. Rossmeisl, A. Logadottir, J.K. Nørskov, Chem. Phys. 319 (2005) 178–184.

[55] M. Zhong, T. Hisatomi, Y. Kuang, J. Zhao, M. Liu, A. Iwase, Q. Jia, H. Nishiyama, T. Minegishi, M. Nakabayashi, N. Shibata, R. Niishiro, C. Katayama, H. Shibano, M. Katayama, A. Kudo, T. Yamada, K. Domen, J. Am. Chem. Soc.

137 (2015) 5053–5060.

[56] D. Cibrev, M. Jankulovska, T. Lana-Villarreal, R. Gómez, Int. J. Hydrogen Energy. 38 (2013) 2746–2753.

[57] M. Amjad, D. Pletcher, C. Smith, J. Electrochem. Soc. 124 (1977) 203–206.

[58] J. Kaulen, H. J. Schäfer, Tetrahedron. 38 (1982) 3299–3308.

[59] B. E. Conway, M. A. Sattar, D. Gilroy, Electrochim. Acta. 14 (1969) 677–694.

[60] B. Ballarin, R. Seeber, D. Tonelli, A. Vaccari, J. Electroanal. Chem. 463 (1999) 123–127.

[61] V. Ganesh, S. Farzana, S. Berchmans, J. Power Sources. 196 (2011) 9890–9899.

[62] D. Wang, W. Yan, G.G. Botte, Electrochem. Commun. 13 (2011) 1135–1138.

[63] A. Andreev, V. Ivanova, K. Kirilov, G. Passage, Appl. Catal. A, Gen. 107 (1994) 189–199.

[64] L. Trotochaud, S. L. Young, J. K. Ranney, S. W. Boettcher, J. Am. Chem. Soc. 136 (2014) 6744–6753.

[65] Y. L. Lo, B. J. Hwang, J. Electrochem. Soc. 142 (1995) 445–450.

[66] D. Pletcher, J. Appl. Electrochem. 14 (1984) 403–415.

[67] P. Cox, D. Pletcher, J. Appl. Electrochem. 20 (1990) 549–554.

[68] K. Kinoshita, Electrochemical oxygen technology, Wiley-Interface, New York, 1992.

[69] M. F. Lichterman, K. Sun, S. Hu, X. Zhou, M. T. McDowell, M. R. Shaner, M. H. Richter, E. J. Crumlin, A. I. Carim, F. H. Saadi, B. S. Brunschwig, N. S. Lewis, Catal. Today. 262 (2016) 11–23.

[70] J. Quiñonero, T. Lana–Villarreal, R. Gómez, Appl. Catal. B Environ. 194 (2016) 141–149.

[71] E. Kádár, L. Sors, S. Kulcsár, E. Kánya, Thermochim. Acta. 107 (1986) 27–35.

[72] K.S. Kim, Surf. Sci. 43 (1974) 625-643.

[73] M. C. Biesinger, B. P. Payne, L. W. M. Lau, A. Gerson, R. S. C. Smart, Surf. Interface Anal. 41 (2009) 324–332.

[74] A. P. Grosvenor, M. C. Biesinger, R. S. C. Smart, N. S. McIntyre, Surf. Sci. 600 (2006) 1771–1779.

Figure captions.

Figure 1. Cyclic voltammograms (scan rate: 10 $mV \cdot s^{-1}$) in the dark for $BiVO_4/Ni(OH)_2$ (black line) and FTO/$Ni(OH)_2$ electrodes (red line), corresponding to deposition times of (a) 10 min, (b) 20 min, (c) 30 min, (d) 40 min and (e) 50 min. Insets in (a) and (b): detail of the voltammetric curves in the high potential region.

Figure 2. (a) Charge density associated with the NiOOH reduction peak *vs.* $Ni(OH)_2$ deposition time, for $BiVO_4/Ni(OH)_2$ (black line) and FTO/$Ni(OH)_2$ electrodes (red line). (b) Current density attributable to the oxygen evolution reaction in the dark, measured at 0.9 V *vs.* the charge density associated to the NiOOH reduction peak, for $BiVO_4/Ni(OH)_2$ (black line) and FTO/$Ni(OH)_2$ electrodes (red line).

Figure 3. Linear scan voltammograms (scan rate: 5 $mV \cdot s^{-1}$) under transient electrolyte-electrode illumination (100 $mW \cdot cm^{-2}$, approx.) for (a-c) $BiVO_4/Ni(OH)_2$, (d-f) La (1 at%)-$BiVO_4/Ni(OH)_2$ and (g-i) Ce (2 at%)-$BiVO_4/Ni(OH)_2$ photoanodes, prepared for different $Ni(OH)_2$ deposition times (0, 20 and 30 min).

Figure 4. Chronoamperometric experiments under transient electrolyte-electrode illumination (100 $mW \cdot cm^{-2}$, approx.) at -0.5 V for $BiVO_4/Ni(OH)_2$ photoanodes corresponding to deposition times of (a) 10 min, (b) 20 min and (c) 30 min. (d) Photocurrent density for the OER at -0.5 V for $BiVO_4/Ni(OH)_2$ photoanodes, prepared with different $Ni(OH)_2$ deposition times (from 0 to 50 min) *vs*. the charge density corresponding to the reduction of NiOOH (and *vs.* the $Ni(OH)_2$ coverage on the electrode surface).

Figure 5. FESEM images corresponding to top views of a (a) bare $BiVO_4$ photoanode and $BiVO_4/Ni(OH)_2$ photoanodes for $Ni(OH)_2$ deposition times of (b) 10 min (pre-optimal), (c) 20 min (optimal) and (d) 30 min (post-optimal). The encircled area in (5d) shows the existence of small particles of deposited $Ni(OH)_2$. TEM images corresponding to a bare $BiVO_4$ photoanode (e) and $BiVO_4/Ni(OH)_2$ photoanodes for $Ni(OH)_2$ deposition times of (f) 10 min, (g) 20 min and (h) 30 min.

Figure 6. Diagram of the mechanism through which the $Ni(OH)_2$ deposit acts as a co-catalyst for the oxygen evolution reaction. A thicker line indicates a higher flow of photogenerated holes.

Figure 7. Cyclic voltammograms (scan rate: 10 $mV \cdot s^{-1}$) in the dark for (a) $BiVO_4/Ni(OH)_2$, (b) La (1 at%)-doped $BiVO_4/Ni(OH)_2$ and (c) Ce (2 at%)-doped $BiVO_4/Ni(OH)_2$ thin film photoanodes prepared with a deposition time of 20 min, before (black line) and after (red line) their photoelectrochemical characterization.

Figure 8. Ni 2*p* XPS spectra for (a) $BiVO_4/Ni(OH)_2$, (b) La (1 at%)-$BiVO_4/Ni(OH)_2$ and (c) Ce (2 at%)-$BiVO_4/Ni(OH)_2$ photoanodes, prepared with a $Ni(OH)_2$ deposition time of 20 min.

Figure 9. (a) FESEM image corresponding to a top view of a $FeVO_4$ photoanode. (b) Cyclic voltammogram (scan rate: 10 $mV \cdot s^{-1}$) in the dark (black line) and linear scan voltammogram (scan rate: 5 $mV \cdot s^{-1}$) under transient electrolyte-electrode illumination (100 $mW \cdot cm^{-2}$, approx.) (red line) for a $FeVO_4$ thin film photoanode.

Figure 10. (a-e) Cyclic voltammograms (scan rate: 10 $mV \cdot s^{-1}$) in the dark and (f-j) linear scan voltammograms (scan rate: 5 $mV \cdot s^{-1}$) under transient electrolyte-electrode illumination (100 $mW \cdot cm^{-2}$, approx.) for $FeVO_4/Ni(OH)_2$ electrodes corresponding to $Ni(OH)_2$ deposition times of (a, f) 10 min, (b, g) 20 min, (c, h) 30 min, (d, i) 40 min and (e, j) 50 min. Red line in (g) corresponds to the linear scan voltammogram for a bare $FeVO_4$ photoanode.

Figure 11. Photocurrent density for the OER at 0.1 V for $FeVO_4/Ni(OH)_2$ photoanodes, prepared with different $Ni(OH)_2$ deposition times (from 0 to 50 min) *vs*. the charge density corresponding to the reduction of NiOOH (and the $Ni(OH)_2$ coverage on the electrode surface).

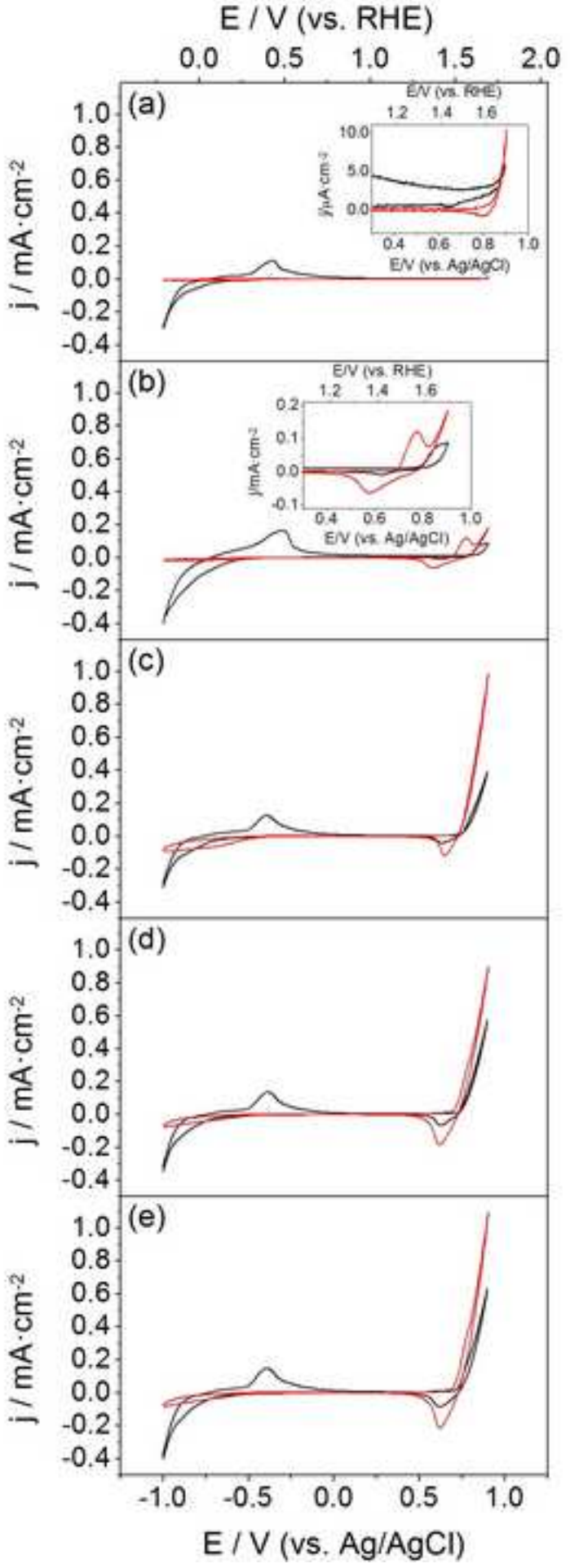

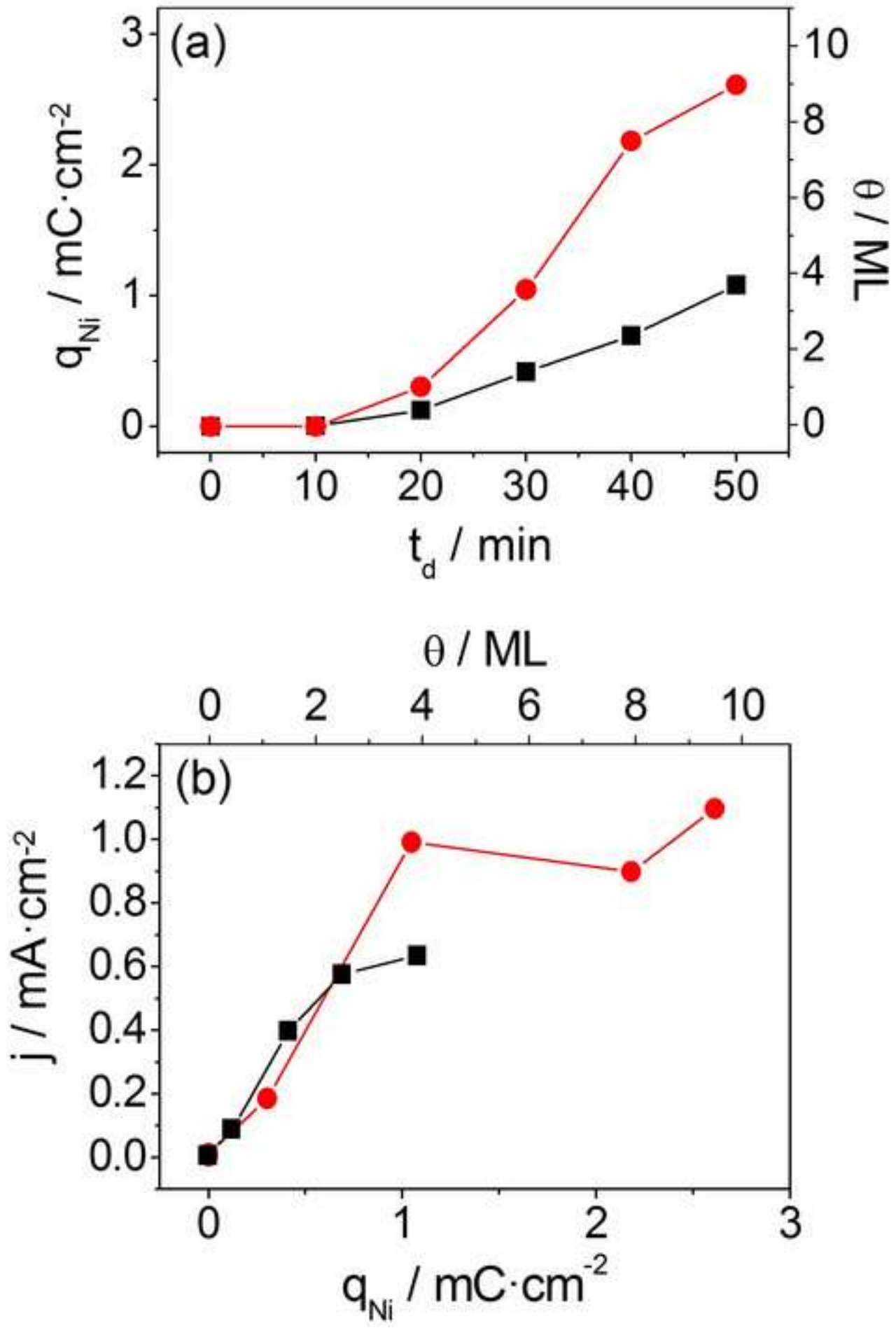

Figure 3

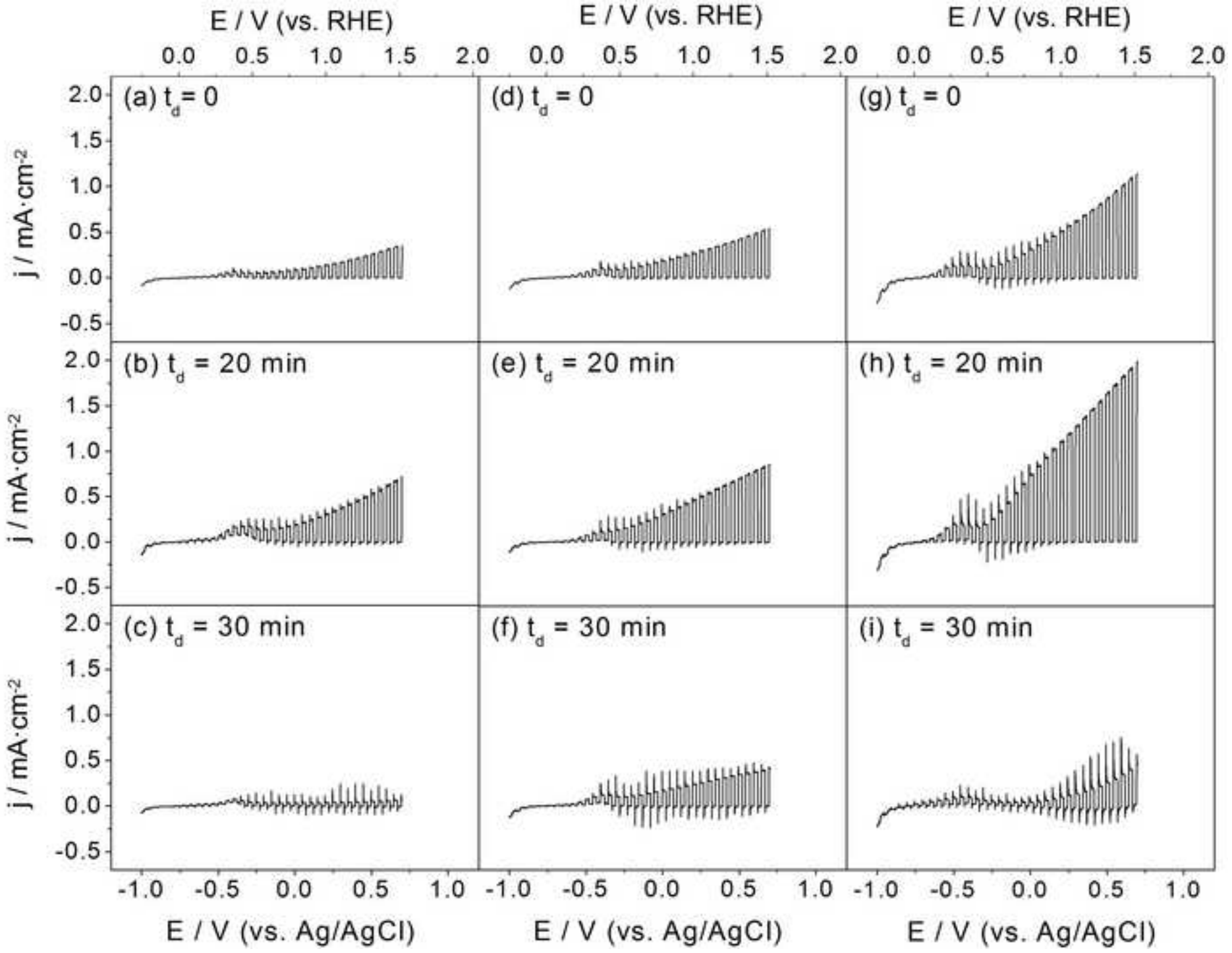
E / V (vs. RHE)
0.0 0.5 1.0 1.5 2.0
(a) t_d = 0
(d) t_d = 0
(g) t_d = 0
(b) t_d = 20 min
(e) t_d = 20 min
(h) t_d = 20 min
(c) t_d = 30 min
(f) t_d = 30 min
(i) t_d = 30 min
j / mA·cm^{-2}
2.0 1.5 1.0 0.5 0.0 -0.5
-1.0 -0.5 0.0 0.5 1.0
E / V (vs. Ag/AgCl)

Figure 4

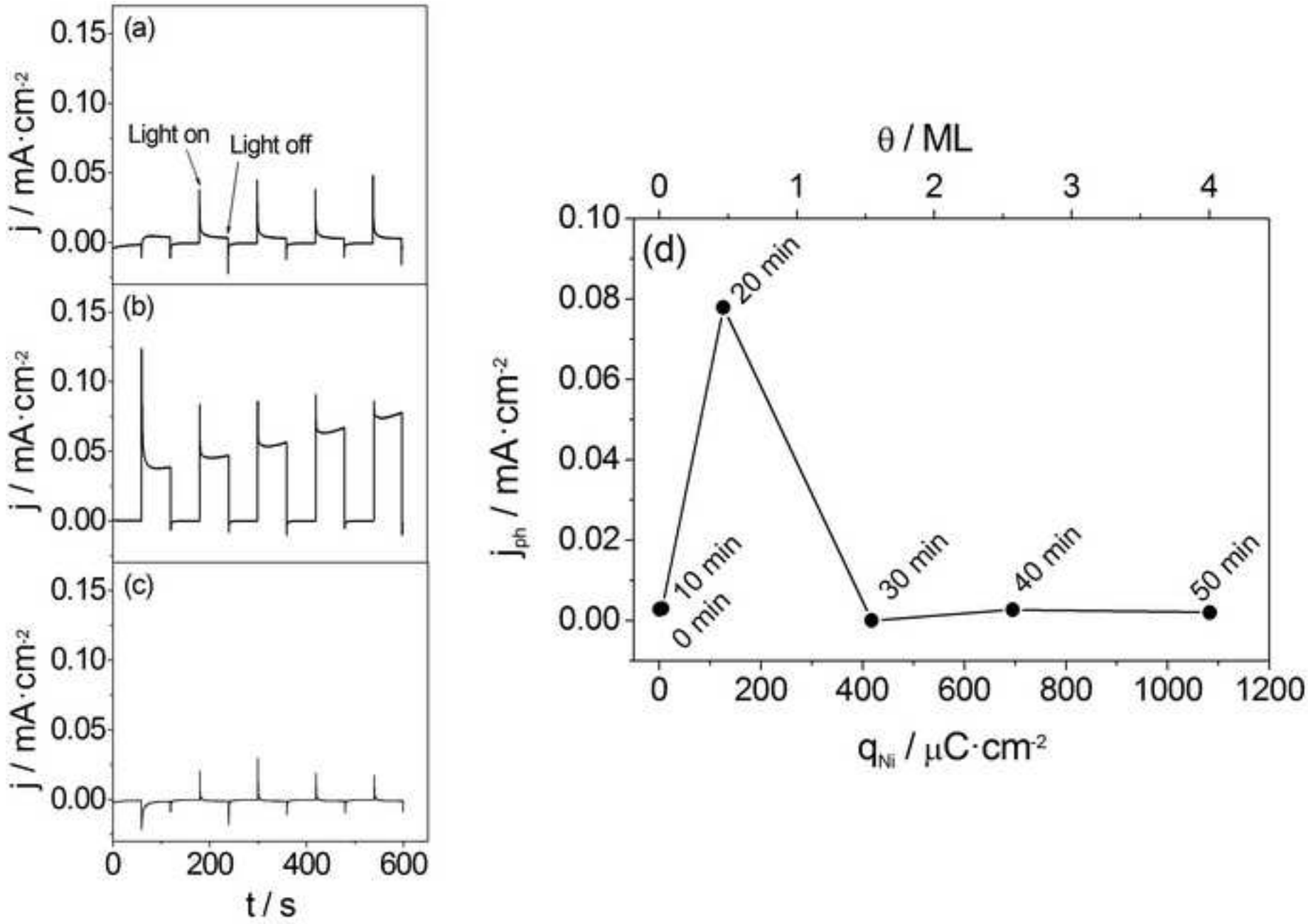
(a)
(b)
(c)
(d)
Light on
Light off
j / mA·cm⁻²
t / s
θ / ML
j_{ph} / mA·cm⁻²
q_{Ni} / μC·cm⁻²
0 min
10 min
20 min
30 min
40 min
50 min

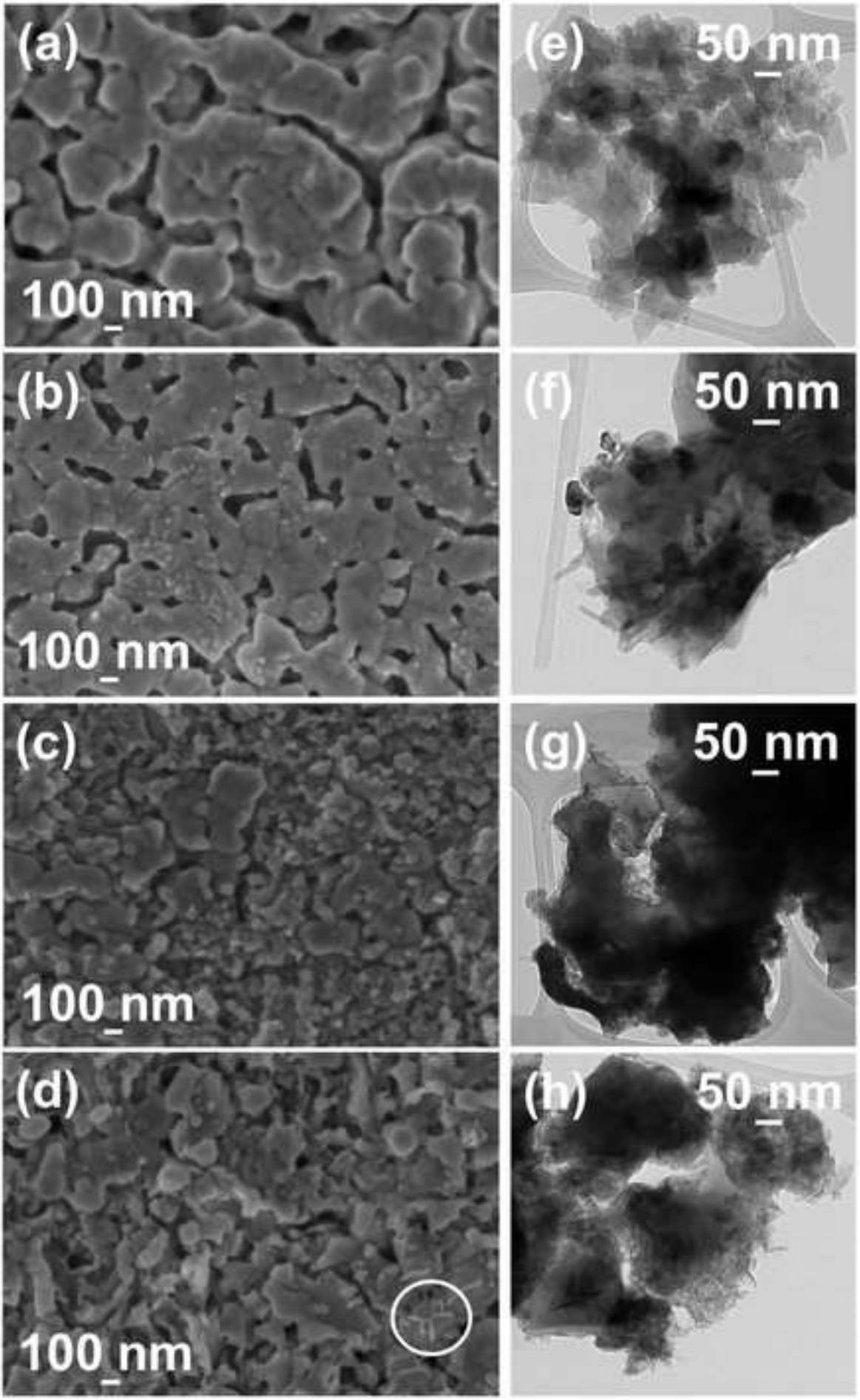

Figure 6

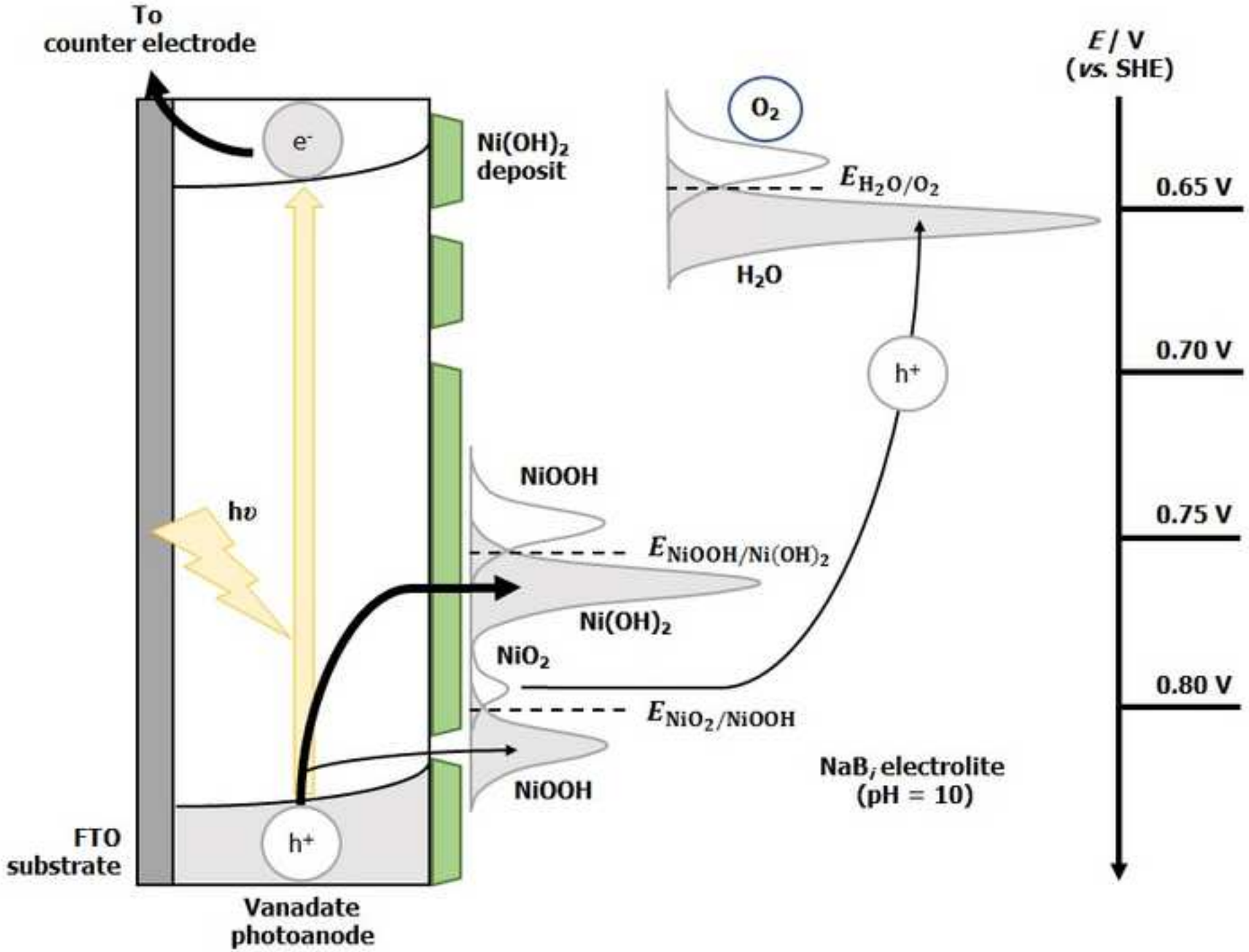
To
counter electrode
e⁻
Ni(OH)₂
deposit
hυ
FTO
substrate
h⁺
Vanadate
photoanode
O₂
E_{H_2O/O_2}
H₂O
h⁺
NiOOH
$E_{NiOOH/Ni(OH)_2}$
Ni(OH)₂
NiO₂
$E_{NiO_2/NiOOH}$
NiOOH
NaBᵢ electrolite
(pH = 10)
E / V
(vs. SHE)
0.65 V
0.70 V
0.75 V
0.80 V

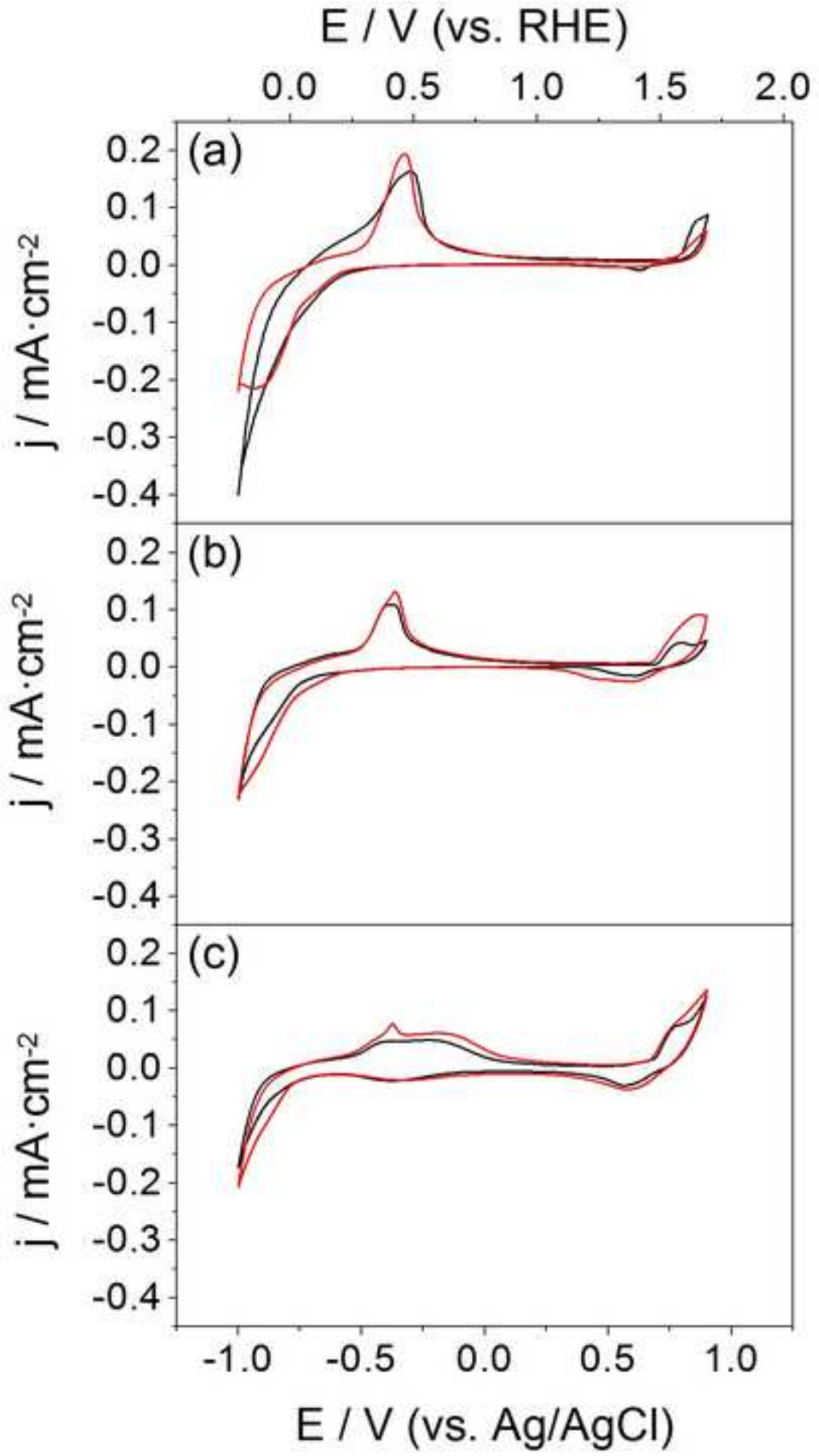

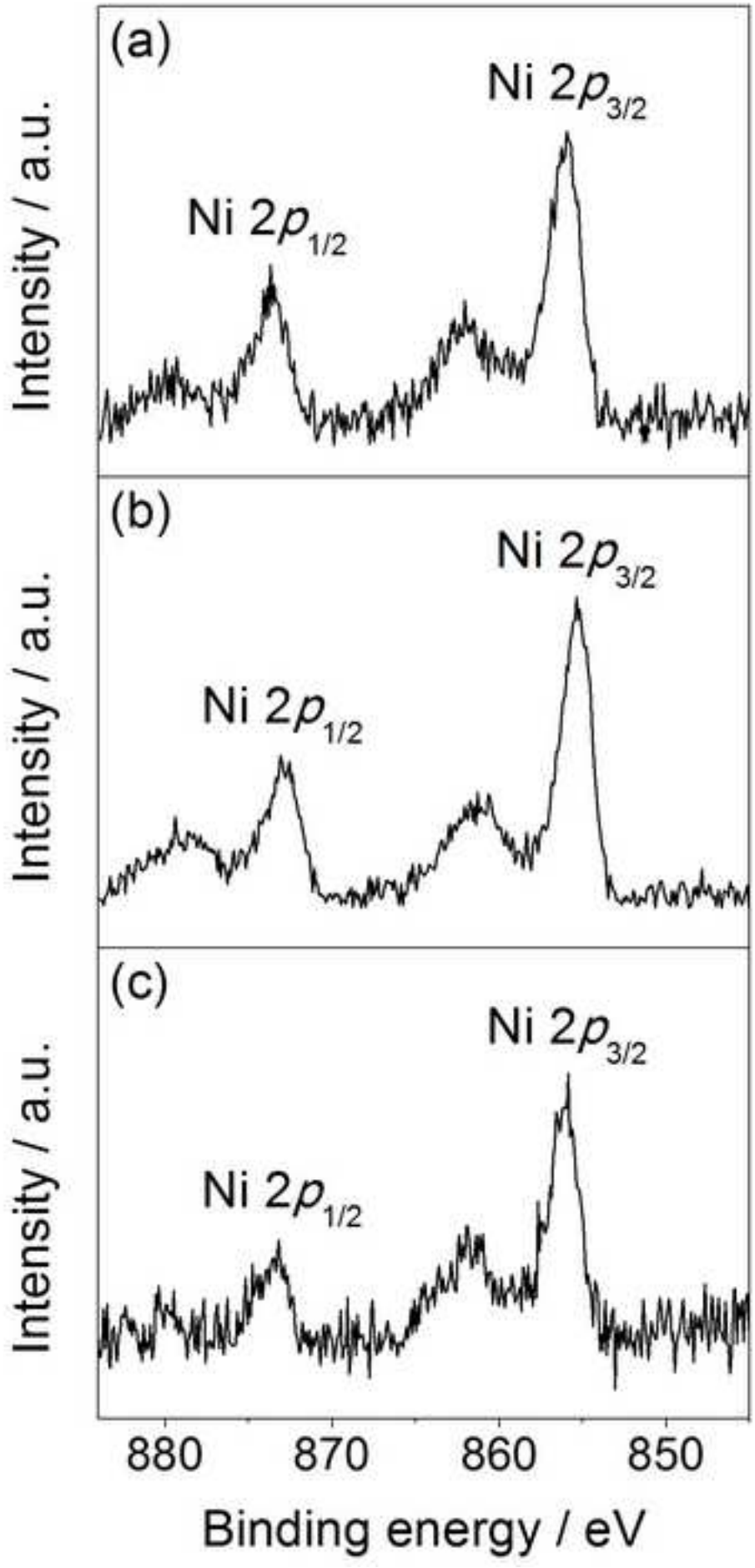

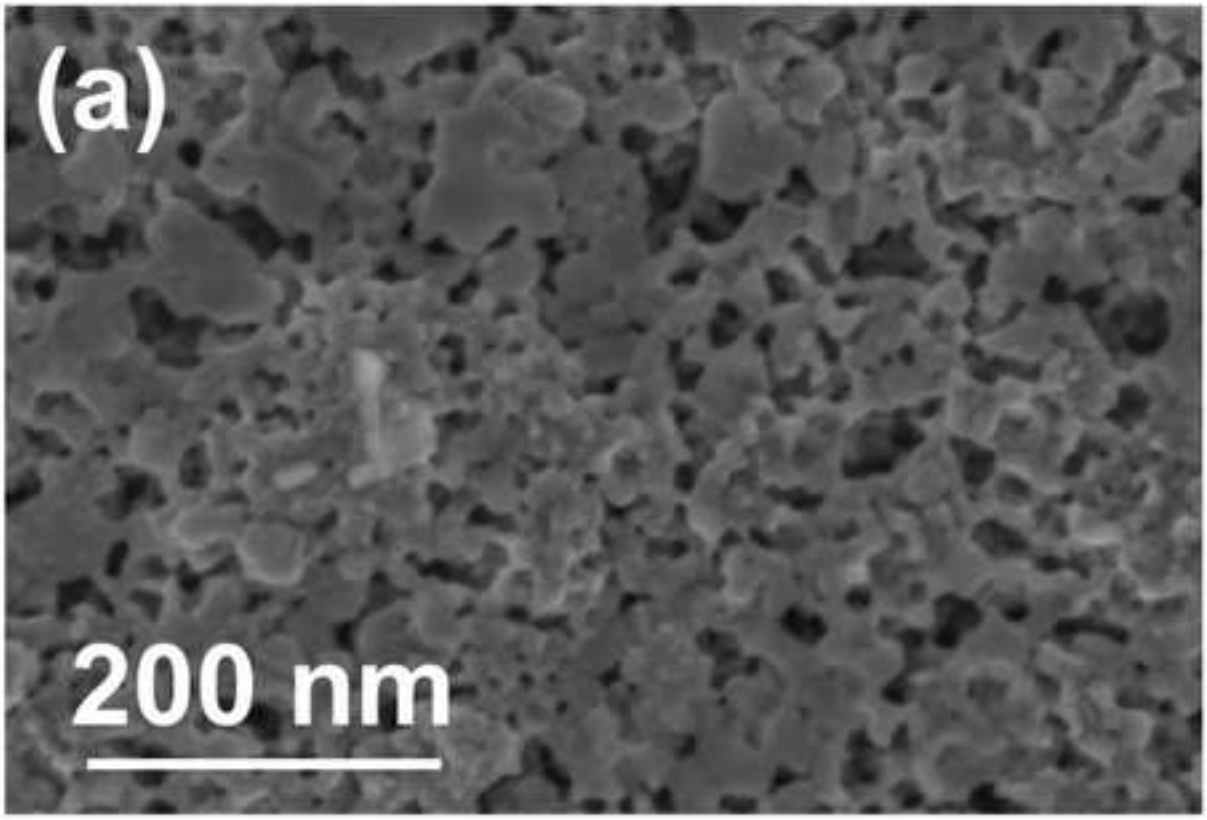

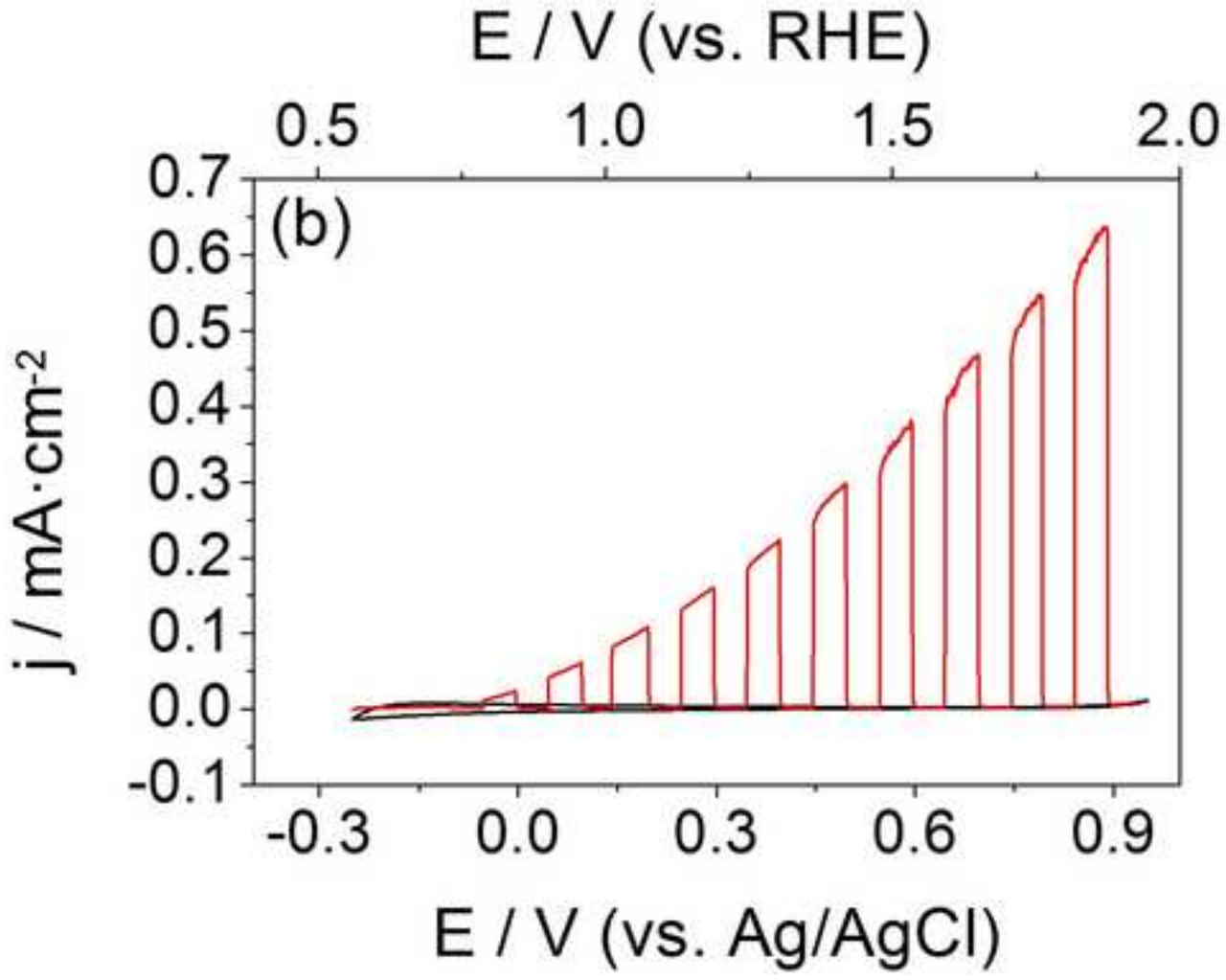

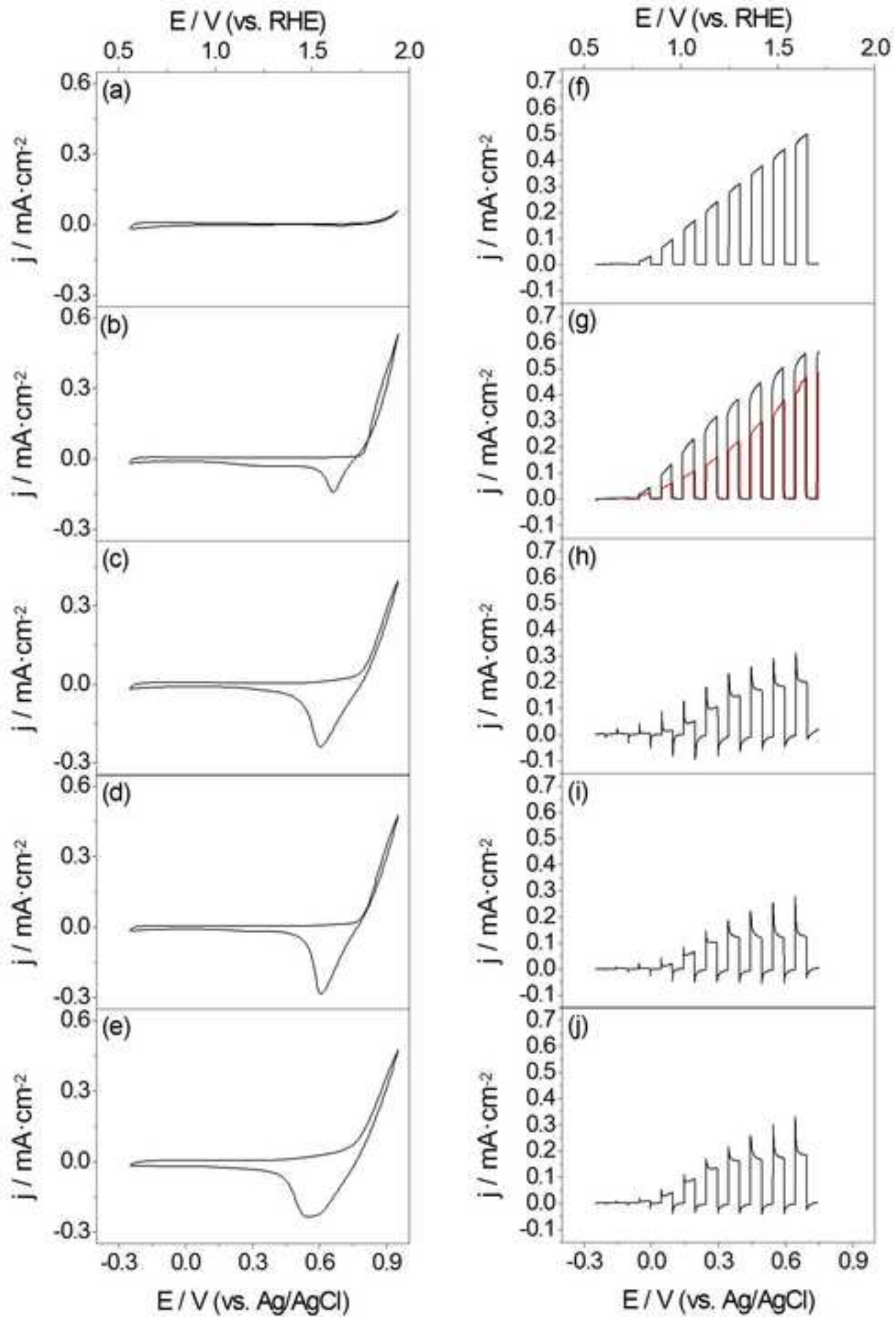

Figure 11

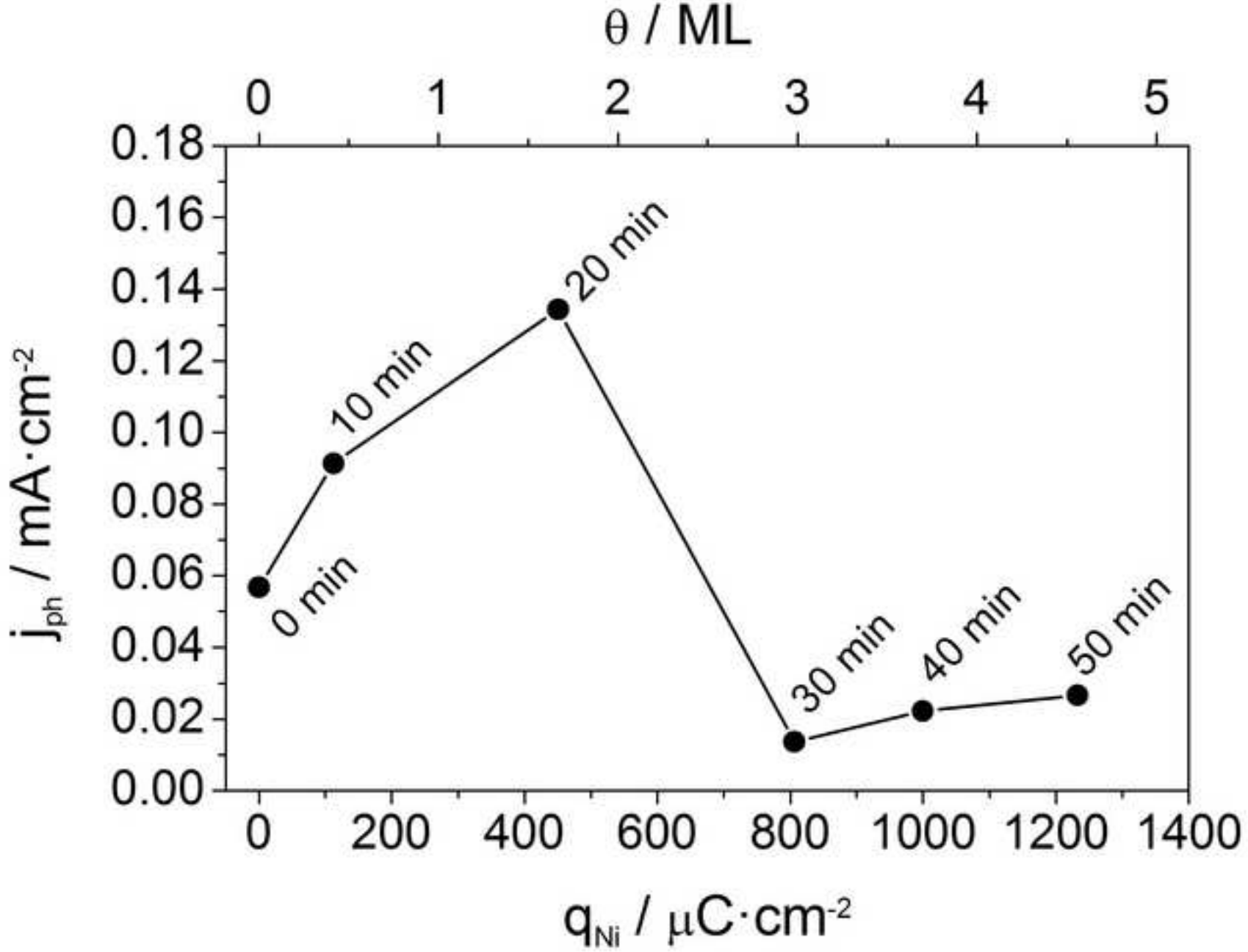
θ / ML
0
1
2
3
4
5
0.18
0.16
0.14
0.12
0.10
0.08
0.06
0.04
0.02
0.00
j_{ph} / mA·cm^{-2}
0 min
10 min
20 min
30 min
40 min
50 min
0
200
400
600
800
1000
1200
1400
q_{Ni} / μC·cm^{-2}

*Graphical Abstract